Article

Design of High Performance Permanent-Magnet Synchronous Wind Generators

Chun-Yu Hsiao *, Sheng-Nian Yeh and Jonq-Chin Hwang

Department of Electrical Engineering, National Taiwan University of Science and Technology, Taipei 10607, Taiwan; E-Mails: snyeh@mail.ntust.edu.tw (S.-N.Y.); jchwang@ee.ntust.edu.tw (J.-C.H.)

* Author to whom correspondence should be addressed; E-Mail: D9607101@mail.ntust.edu.tw; Tel.: +886-9-2113-5781; Fax: +886-2-2737-6699.

Abstract: This paper is devoted to the analysis and design of high performance permanent-magnet synchronous wind generators (PSWGs). A systematic and sequential methodology for the design of PMSGs is proposed with a high performance wind generator as a design model. Aiming at high induced voltage, low harmonic distortion as well as high generator efficiency, optimal generator parameters such as pole-arc to pole-pitch ratio and stator-slot-shoes dimension, *etc.* are determined with the proposed technique using Maxwell 2-D, Matlab software and the Taguchi method. The proposed double three-phase and six-phase winding configurations, which consist of six windings in the stator, can provide evenly distributed current for versatile applications regarding the voltage and current demands for practical consideration. Specifically, windings are connected in series to increase the output voltage at low wind speed, and in parallel during high wind speed to generate electricity even when either one winding fails, thereby enhancing the reliability as well. A PMSG is designed and implemented based on the proposed method. When the simulation is performed with a 6 Ω load, the output power for the double three-phase winding and six-phase winding are correspondingly 10.64 and 11.13 kW. In addition, 24 Ω load experiments show that the efficiencies of double three-phase winding and six-phase winding are 96.56% and 98.54%, respectively, verifying the proposed high performance operation.

1. Introduction

The permanent-magnet synchronous generator (PMSG), which is less noisy, high efficiency and has a long life span, has becomes one of the most important types of equipment in wind turbine systems. In 2008, Bumby designed and fabricated a 5 kW, 150 rpm axial vertical permanent-magnet (PM) generator driven directly by wind and a water turbine, where the generator uses trapezoidal shaped magnets to enhance the magnetism over conventional circular magnets. The average efficiency is 94% under no core losses and only limited eddy current loss [1]. In 2011, Maia used finite element method (FEM) software to analyse the operation characteristics of an axial PM wind turbine with rated output power of 10 kW while running at the speed of 250 rpm [2]. He [3] indicated that the electromagnetic properties of the permanent-magnet machine are highly dependent on the number of slots per pole, phase, magnet shape, the stator slots and the slot opening. Eriksson described that a winding scheme having slots per pole ratio of 5/4 will reduce the cogging torque and suppress unwanted harmonics. The third harmonic distortion measured is 5.8% under no-load and load of a 12 kW direct driven PM synchronous generator [4]. Erickson also designed a PM generator rated at 10 kW of telecommunication tower. The generator's electrical efficiency is 94.3% using a 2-D FEM model simulation [5]. From the literature to date, a systematic procedure and methodology concerning the determination of optimal structural parameters of PM wind generator leading to desired efficiency seems lacking. This motivated the study of this paper.

Axial flux PMSGs are widely used for vertical-axis wind turbines [6–10], however, since the axial structure magnet is placed on the inner surface of the rotor without slot and facing the stator, it will lengthen the distance between upper and lower magnets, which in turn requires much more magnet material and cost to improve the operational efficiency.

This paper adopts the radial flux type PMSG, which has its stator windings placed in the inner core, needs less magnet, and therefore resulting in cost reduction as well as heat loss elimination. In addition, it applies vertical-axis wind turbine and direct drive structure and blade coupling generator. Therefore it doesn't need to speed up/slow down the gearbox to decrease the noise caused and reduce the machinery wastage. It also presents a systematic approach for the design of permanent-magnet synchronous wind generator. To exemplify the feasibility of the proposed methodology, analysis and design of a high performance, multi-pole, gearless PMSG aiming at high efficiency and low voltage harmonics simultaneously using less material and having lighter structure is given. In addition, a novel six stator winding structure is also proposed to yield versatile applications. During low wind speed, the two three-phase windings are connected in series to increase the output voltage, while at high wind speed, the six windings are connected in parallel to provide more current and ensure power continuity when either one of the two three-phase windings fails [11].

The paper is organized as follows: Section 2 is concerned with the dimension of rotor design; Section 3 describes the use of Maxwell 2-D to determine the suitable ratio of pole-arc to pole-pitch, and the use of the Taguchi method to find the stator-slot-shoes dimension; the designed parameters for high

performance PMSG is also given in this section. Section 4 presents experimental results and their comparison with Maxwell 2-D simulations; finally, conclusions are given in Section 5.

2. Design Dimension of the Rotor

Both the designed double three-phase and six-phase winding configurations of PMSG consist of six composite windings with the advantage of high conductor utilization rate and lower torque ripple [11]. Meanwhile, it can disperse the armature current evenly under the same voltage and power conditions.

Figure 1 shows a simple and generally used surface mount with the basic geometric structure. It has a complete magnetic flux circuit, half N-pole and half S-pole, the magnetic flux travels from the rotor surface through the airgap, the magnetic silicon steel in the stator, the airgap, and then back to the rotor to form a complete closed-loop.

Figure 1. Schematic diagram of permanent-magnet synchronous generator (PMSG): magnetic flux path.
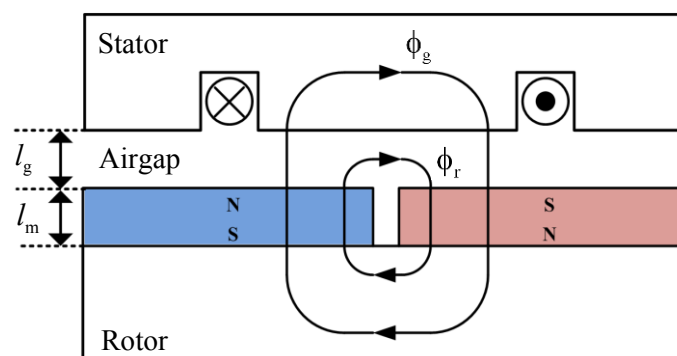
The equivalent magnetic circuit can be modeled as shown in Figure 2a. The stator yoke width should be selected properly for reducing flux leakage and preventing magnetic saturation due to too small width of the yoke, or over weight and dimension coming from thicker yoke [12].

Figure 2. A magnetic circuit model for the proposed structure: (**a**) complete magnetic circuit model; (**b**) simplified magnetic circuit model.
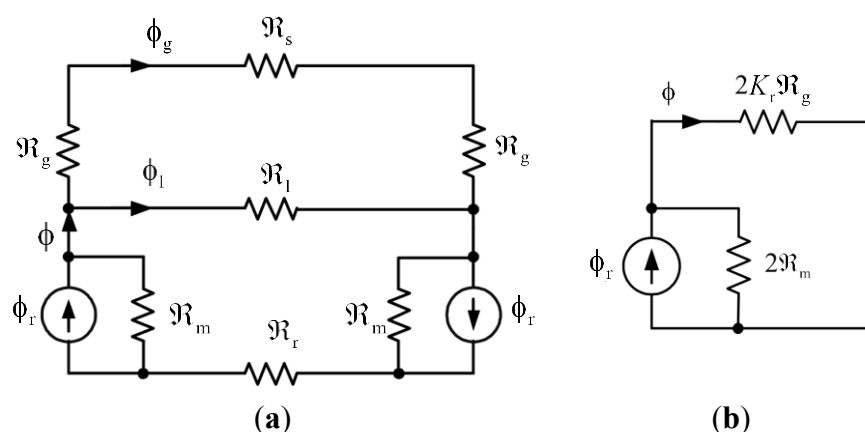
The airgap flux can be written as $\phi_g = K_l \cdot \phi$, where the leakage factor K_l is typically less than unity. For rapid analysis of the magnetic circuit, leakage magnetic reluctance $\mathfrak{R}_l$ is ignored as shown in

Figure 2b. In addition, since the steel reluctance ($\Re_r + \Re_s$) is small relative to the airgap reluctance $\Re_g$, the steel reluctance can be eliminated by introducing a reluctance factor K_r having its value chosen to be a constant slightly greater than unity to multiply the $\Re_g$ to account for the neglected ($\Re_r + \Re_s$). For the machine with surface magnets under consideration, the leakage and reluctance factors are typically in the ranges of 0.9–1.0 and 1.0–1.2, respectively, while the flux concentration factor is ideally 1.0.

The magnetic flux can be derived as [12]:

$$\phi = \frac{\phi_r \, 2\Re_m}{2\Re_m + 2\Re_g + \Re_s + \Re_r} = \frac{\phi_r \, 2\Re_m}{2\Re_m + 2K_r\Re_g} = \frac{\phi_r}{1 + K_r \dfrac{\Re_g}{\Re_m}} \tag{1}$$

Since the relationship between permeance coefficient (P_c) and airgap flux density is nonlinear, doubling P_c does not double B_g. Doubling P_c, however, means doubling the magnet length, which doubles its volume and associated cost accordingly. Using the relation:

$$P_c = \frac{l_m A_g}{l_g A_m} \tag{2}$$

and:

$$\Re_m = \frac{l_m}{\mu_r \mu_0 A_m}, \quad \Re_g = \frac{l_g}{\mu_0 A_g}, \quad B_g = \frac{\phi_g}{A_g}, \quad B_r = \frac{\phi_r}{A_m} \tag{3}$$

Equation (1) becomes:

$$B_g A_g = \frac{B_r A_m}{1 + K_r \dfrac{\mu_r}{P_c}} \tag{4}$$

Assuming that all the magnetic fluxes leaving the magnet through an airgap go into the stator core, then:

$$A_g = A_m \tag{5}$$

Since, as indicated above, K_r is slightly greater than unity, it is further assumed that $K_r = 1$. Thus, substituting Equation (5) into Equation (4) results in:

$$\frac{B_g}{B_r} = \frac{1}{1 + \mu_r \dfrac{l_g}{l_m}} \tag{6}$$

Determination of the airgap length l_g depends on the gap magnetic flux density and the processing of machine structure. If the airgap length is too short, it will cause serious eccentric force at high speed. Wider airgap length, however, will reduce the gap magnetic flux density and lower efficiency. The optimal ratio between magnet thickness and the airgap is usually selected in the range of 4–6 as shown in Figure 3 [12]. Usually generator designer determines magnet thickness in accordance with this search range. Meanwhile, production and installation tolerances must be considered to decide the eventual airgap length in order

to avoid motor assembly complexity and operating problems. Equation (6) will be used to decide the initial airgap length shown in Table 2 of Section 3.

Figure 3. Relationship between normalized airgap flux density and permeance coefficient.
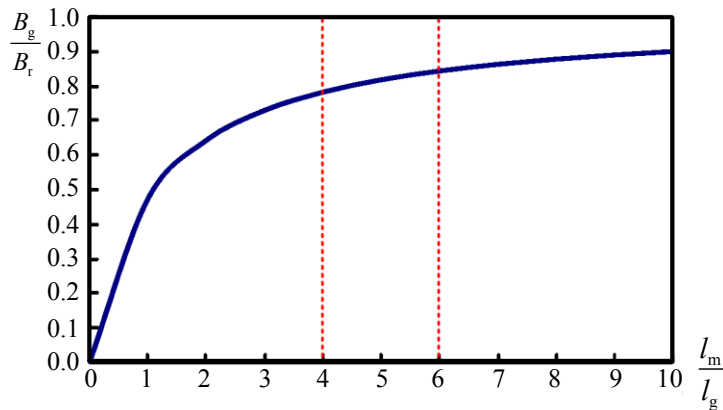
Ignoring the magnetic effects caused by the stator teeth, the distribution of airgap flux density can be illustrated by Figure 4. The ratio α_{p-p} [13] between the width of the magnet and the pole-pitch of rotor core, written as the ratio of pole-arc α_{arc} to pole-pitch α_{pitch}, is defined in Equation (7), where α_{arc} and α_{pitch} are the angular span of any single magnet and that between the center lines of any two adjacent magnetic poles, respectively. It is related to flux density. Specifically, the greater ratio, *i.e.*, the longer magnet arc length, will result in higher flux density. If the gap magnetic flux density waveform is closer to sinusoidal, then the induced voltage harmonics content will be smaller:

$$\alpha_{p-p} = \frac{\alpha_{arc}}{\alpha_{pitch}} \tag{7}$$

when α_{p-p} is unity, the N and S poles of the magnet are consecutive, *i.e.*, without a gap in between, the gap flux density is a square wave. In general, for $0 \leq \alpha_{p-p} \leq 1$, Fourier series expansion of the flux density at any electrical degree θ_e in the airgap can be derived as:

$$B_g = \frac{2B_{g,peak}}{\pi} \sum_{k_h=1}^{\infty} \frac{1-(-1)^{k_h}}{k_h} \cos[k_h(\frac{1-\alpha_{p-p}}{2})\times180°]\sin k_h\theta_e \tag{8}$$

where $B_{g,peak}$ is the maximum flux density of airgap and k_h is the *k*-th harmonic.

Figure 4. Relationship between α_{p-p} and airgap flux density: (**a**) $\alpha_{p-p} = 1$; (**b**) $\alpha_{p-p} = 0.5$.
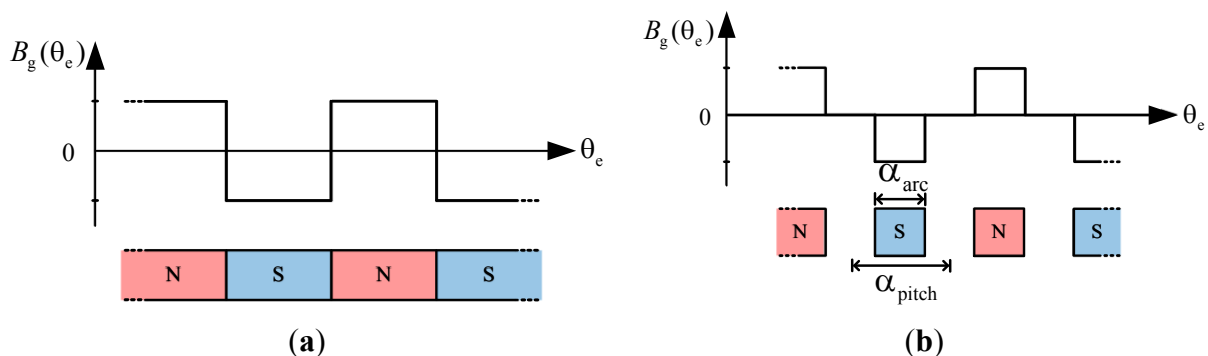
Equation (8) yields the *k*-th harmonic flux ratio:

$$B_{k_h} = \frac{1-(-1)^{k_h}}{k_h} \cos[k_h(\frac{1-\alpha_{p-p}}{2}) \times 180°] \tag{9}$$

It is seen from Equation (9) that the airgap flux density ratio of harmonic is determined by different α_{p-p}, as shown in Table 1. For balanced three-phase, the third harmonic can be eliminated by using Y-connected wiring. The harmonic distortion is not proportional to the phase and line voltages, but depends on the third harmonic of the phase voltage. Even if the third harmonic of the phase voltage will not appear in the line voltage, it will cause losses within each phase winding. It is obvious from Table 1 that $\alpha_{p-p} = 0.800$ will yield the smallest 3rd and smaller 5th harmonics. This choice of α_{p-p} for the smallest 5th harmonic will further be confirmed by the finite element analysis given in Section 3.

Table 1. Relationship between α_{p-p} and airgap flux density ratio.

α_{p-p}	$B_{k_h=1}$	Harmonic content ($B_{k_h} / B_{k_h=1, \alpha_{p-p}=1}$)				
		1st (pu)	3rd (pu)	5th (pu)	7th (pu)	11th (pu)
0.667	1.7322	0.8661	0.0000	0.1732	0.1237	0.0788
0.800	1.9022	0.9511	0.1960	0.0000	0.0840	0.0865
0.857	1.9498	0.9749	0.2605	0.0866	0.0000	0.0712
0.909	1.9796	0.9898	0.3032	0.1511	0.0771	0.0000
1.000	2.0000	1.0000	0.3333	0.2000	0.1429	0.0909

3. Simulation Results and Discussion

The finite element method from the Maxwell-2D software will be used throughout the analysis and design in this section. The relevant specifications and dimensions of the generator under design are listed in Table 2 with the sketched schema graph of PMSG and magnet dimensions given in Figure 5. As will be illustrated in the following, to design PMSG for double three-phase and six-phase winding connections, α_{p-p} will first be determined to obtain the greatest induced voltage and its smallest harmonic content.

Figure 5. Schema graph of PMSG and magnet dimension: (**a**) structure of a 78-pole, 72-slot PMSG; (**b**) magnet dimension.

(**a**)   (**b**)
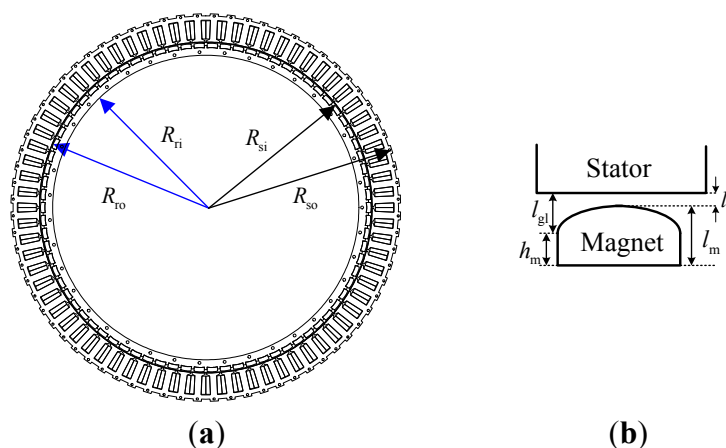
The optimal size of the stator shoes is then decided by using the Taguchi method. Moreover, the induced voltage and current values can be determined by using different loads at the specific rotor speed and then calculate power output. Maxwell_2D and Fourier transform are applied to analyze PSMG-based electrical characteristics.

Table 2. Parameters of wind generator to be designed.

Parameter	Value
Pole number	78
Slot number	72
Number of phase	double three-phase and six-phase
Rated speed (rpm)	90
Rated output power (W)	10,000
Rated torque (N·m)	1,061
Induced voltage (V)	150
Estimated efficiency (%)	90
Winding turns per slot (turns)	25
Winding conductor diameter (m)	$(0.0012) \times 4$
Stator radius: inner/outer (m) R_{si}, R_{so}	0.3065/0.3550
Rotor radius: inner/outer (m) R_{ri}, R_{ro}	0.2820/0.3045
Airgap length (m) l_g	0.002
Magnet thickness (m) l_m	0.008
Stack length (m)	0.12
Core material/Permanent magnet	50H400/NdFeB42H
End airgap length of rotor magnet (m) l_{gl}	0.0026

3.1. Optimal Sizing of Rotor Magnet

Aiming at high induced voltage and low harmonic distortion, sizing of rotor magnet will be conducted by the best pole-arc to pole-pitch ratio, α_{p-p}. Fixing the internal and external diameters of stator and rotor as given in Table 2, double three-phase winding are used.

Assuming open stator slot as above, finite element analyses using Maxwell 2-D software for five different α_{p-p}, *i.e.*, $\alpha_{p-p} = 0.667$, 0.800, 0.857, 0.909, and 1.000 are given. Figure 6 shows the various phase voltage V_p and line voltage V_l values obtained by Maxwell 2-D with different α_{p-p}. When $\alpha_{p-p} = 0.800$, the values for V_p and V_l are 243.3 V and 458.4 V, respectively.

Figure 6. Induced voltages of PMSG with different α_{p-p} by Maxwell 2-D: (**a**) Phase voltage; (**b**) Line voltage.

(**a**)   (**b**)
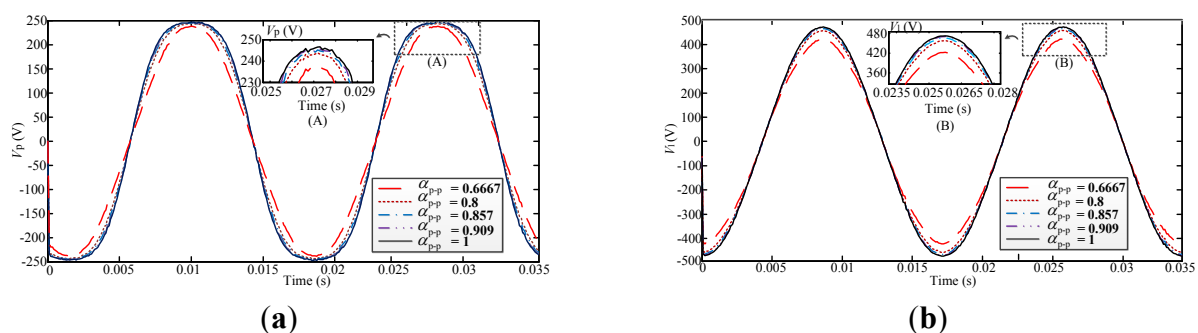
The results shown in Table 3 reveal that $\alpha_{p-p} = 0.800$ will yield the smallest 5th harmonic voltage (0.14/0.13) with sufficiently high induced voltage. This agrees with Table 1 that $\alpha_{p-p} = 0.800$ will yield the smallest 5th and smaller 3rd harmonics. Besides, as mentioned in Section 2 that for balanced three-phase, the third harmonic voltage can be eliminated by using Y-connected wiring.

Table 3. Induced voltages and total harmonic distortion (THD) of 72-slot, 78-pole PMSG with different α_{p-p}.

α_{p-p}	V_p/V_1 (V)	*THD* (%)	Each order harmonic (Phase/Line)				
			3rd	**5th**	**7th**	**9th**	**11th**
0.667	237.7/421.7	1.17/1.18	0.07/0.02	1.11/1.11	0.17/0.22	0.05/0.06	0.01/0.02
0.800	243.3/458.4	7.28/0.41	7.27/0.01	0.14/0.13	0.15/0.19	0.09/0.03	0.02/0.01
0.857	244.8/465.7	9.26/0.54	9.24/0.05	0.25/0.29	0.08/0.07	0.06/0.07	0.03/0.02
0.909	245.6/470.7	10.38/0.67	10.36/0.03	0.46/0.48	0.03/0.03	0.09/0.09	0.12/0.08
1.000	246.7/472.2	11.00/0.72	10.98/0.03	0.60/0.63	0.11/0.07	0.50/0.06	0.05/0.02

3.2. Determining the Optimal Stator-Slot-Shoes Dimension Using Taguchi Method

Conventionally, to find the most appropriate parameters for the optimum design, analyses or tests are usually conducted by changing one factor at a time for each experiment while other factors are kept fixed. The basic principle of Taguchi method is, however, to choose several control factors and use an orthogonal array to get useful statistic information with the fewest experiments. Taguchi method has been widely used in motor design since it provides engineers with a systematic and efficient method to administer numerical experiments and acquire the optimal parameters quickly [14–20].
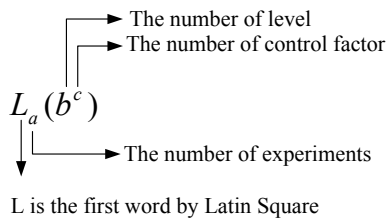
Consider the block diagram shown in Figure 7, where system represents a product or manufacturing process, such as PMSG in our case here, y refers to the quality characteristics or response, signal factors (M), controllable factors (Z) and noise factors (X) are factors that can affect y [16].

Figure 7. Product/process parameters.
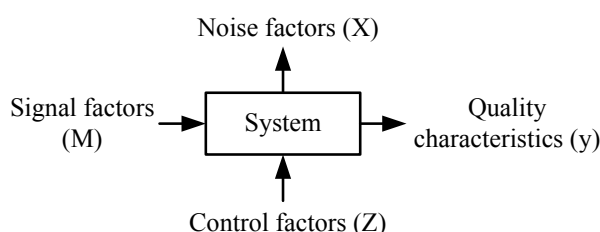
The effect of many different parameters or control factors on the performance characteristic in a condensed set of experiments can be examined by using the orthogonal array experimental design proposed by Taguchi [14,15]. Knowing the number of parameters and the number of levels, the proper orthogonal array can be selected as shown in Table 4, which is adopted in this paper with the slot opening length, the height of the shoe portion, the magnet length, and the tooth width chosen as the control factors.

Table 4. $L_{16}(4^5)$ Array.

The number of level

The number of control factor

$L_a(b^c)$

The number of experiments

L is the first word by Latin Square

Experiment	1	2	3	4	5	6	7	8	9	10	11	12	13	14	15	16
A	1	1	1	1	2	2	2	2	3	3	3	3	4	4	4	4
B	1	2	3	4	1	2	3	4	1	2	3	4	1	2	3	4
C	1	2	3	4	2	1	4	3	3	4	1	2	4	3	2	1
D	1	2	3	4	3	4	1	2	4	3	2	1	2	1	4	3
E	1	2	3	4	4	3	2	1	2	1	4	3	3	4	1	2

One of the key features of Taguchi method is the use of signal-to-noise, *S/N*, ratio to transform the performance characteristic in the optimization process. The signal represents the mean performance while the noise signifies the variance. No matter what the applications, the method of measurement, or the units in which the results are expressed, there can be three types of *S/N* with the criteria: bigger is better, smaller is better and nominal is the best.

Taguchi strongly recommends the use of *S/N* ratio, expressed as a log transformation of the mean-squared deviation, as the yardstick for analysis of experimental results. *i.e.*,

$$y = g(M;Z) + e(X;M;Z) \tag{10}$$

where the signal *g*(*M*; *Z*) and the noise *e*(*X*; *M*; *Z*) are usually in the predictable and unpredictable sections, respectively. The objective of the design is to maximize the predictable and minimize the unpredictable parts, correspondingly.

For the-larger-the-better (LTB) target, the *S/N* ratio is:

$$S/N = -10\log\left[\frac{1}{n}\sum_{i=1}^{n}(\frac{1}{y_i^2})\right] \tag{11}$$

For the-smaller-the-better (STB) quality characteristic, *S/N* ratio is defined as:

$$S/N = -10\log\left[\frac{1}{n}\sum_{i=1}^{n}(y_i^2)\right] \tag{12}$$

The performance index follows LTB for this paper, it can be expressed as:

$$S/N = -10\log(\frac{1}{V_p^2}) - 10\log(THD^2) - 10\log(T_B^2) \tag{13}$$

The first mathematical term can be considered the induced voltage which in value is relatively higher; the next two terms respectively represent the total harmonic distortion (THD) and flux density of tooth width, both having a smaller value.

As mentioned above, four control factors, namely that slot opening length, external height of shoes (Shoes'_ho), internal height of shoes (Shoes' hi) and tooth width are chosen in spite of the fifth control factor [21,22]. Moreover, four levels are applied for each factor to maximize the induced voltage of generator and keep the flux density of stator teeth lying within the saturation point of their laminations. Details are given in the following section.

In this section, the Taguchi method will be used to determine the dimension of stator shoes. Consider Figure 8. Four parameters, slot-opening length, ho, hi, and tooth width are chosen as control factors, which are subdivided into four levels to yield four row data shown in Table 5 for the orthogonal array

$L_{16}(4^5)$ to process 16 simulations with Maxwell-2D and Matlab software. The results for no-load analysis of double three-phase winding configuration are summarized in Table 6 and Figure 9.

Figure 8. Slot dimensions.
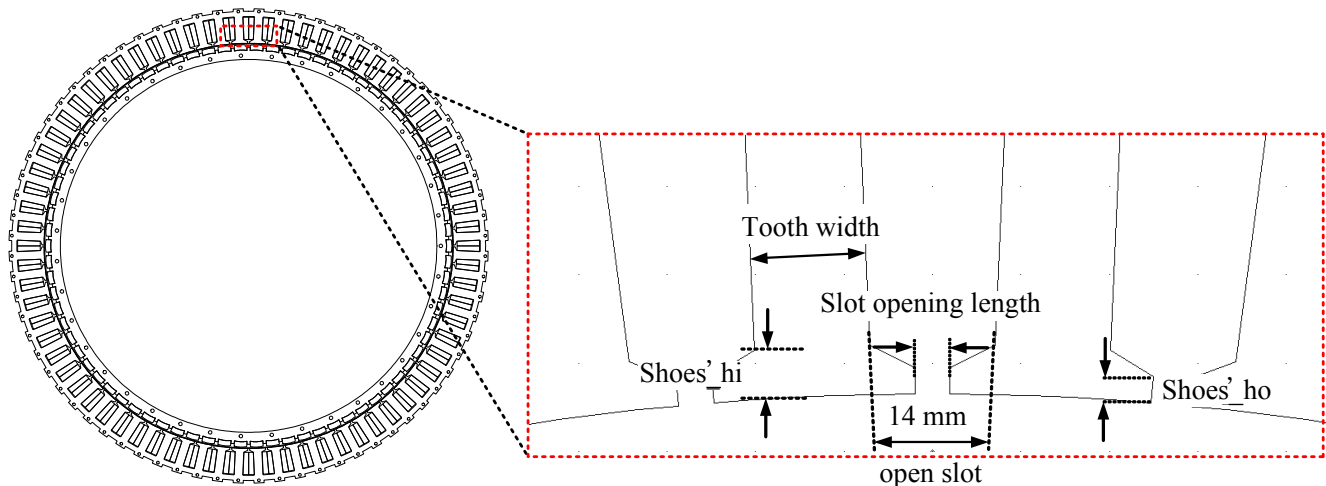
Table 5. Four control factors and levels of stator shoes.

| Level	Control factor			
	A	**B**	**C**	**D**
	Slot opening length (mm)	**Shoes'_ho (mm)**	**Shoes'_hi (mm)**	**Tooth width (mm)**
1	1	0	1	7
2	2	1	2.5	9
3	3	2	4	11
4	4	3	5.5	13

Table 6. Performance statistics for induced voltage, THD and flux density of tooth width. Optimized value: V_p(V): 208, *THD*(%): 0.39, T_B: 1.2655, *S/N*: 52.49.

| No.	1	2	3	4	5	6	7	8
V_p (V)	149	163	191	207	179	185	158	186
THD (%)	1.58	2.69	1.71	0.65	1.84	2.85	3.83	2.18
T_B (Tesla)	1.6489	1.5282	1.3050	1.2582	1.3491	1.2148	1.6823	1.5833
S/N	35.15	31.97	38.65	48.07	37.16	34.56	27.79	34.63
No.	**9**	**10**	**11**	**12**	**13**	**14**	**15**	**16**
V_p (V)	191	192	171	160	174	154	201	197
THD (%)	1.86	1.01	1.29	3.53	1.42	1.99	0.97	1.24
T_B (Tesla)	1.2257	1.1457	1.5825	1.6956	1.5848	1.7199	1.2539	1.4692
S/N	38.46	44.40	38.46	28.54	37.77	33.06	44.36	40.68

Table 6 indicates that the best *S/N* ratio among the 16 simulations is obtained during the 4th run (*S/N* = 48.07), with *THD* and T_B equal to 0.65 and 1.2582, respectively. Besides, It is seen from Figure 9 that the dimensions of slot-opening length, Shoes'_ho, hi, and tooth width for the optimized *S/N* ratio are 4, 3, 5.5 and 13 mm, respectively; the corresponding optimized values are V_p (V): 208, *THD* (%): 0.39, T_B: 1.2655 and *S/N*: 52.49. When 50H400 silicon steel sheet is used with maximum saturation point,

1.6300 Tesla, as a limit, the optimized value from Figure 10 (1.2655 Tesla) still does not exceed the threshold from simulations to avoid producing the problems of high temperature and the demagnetization phenomenon while the flux density of tooth width is near 1.6300 Tesla.

Figure 9. Taguchi analysis for different control factors.
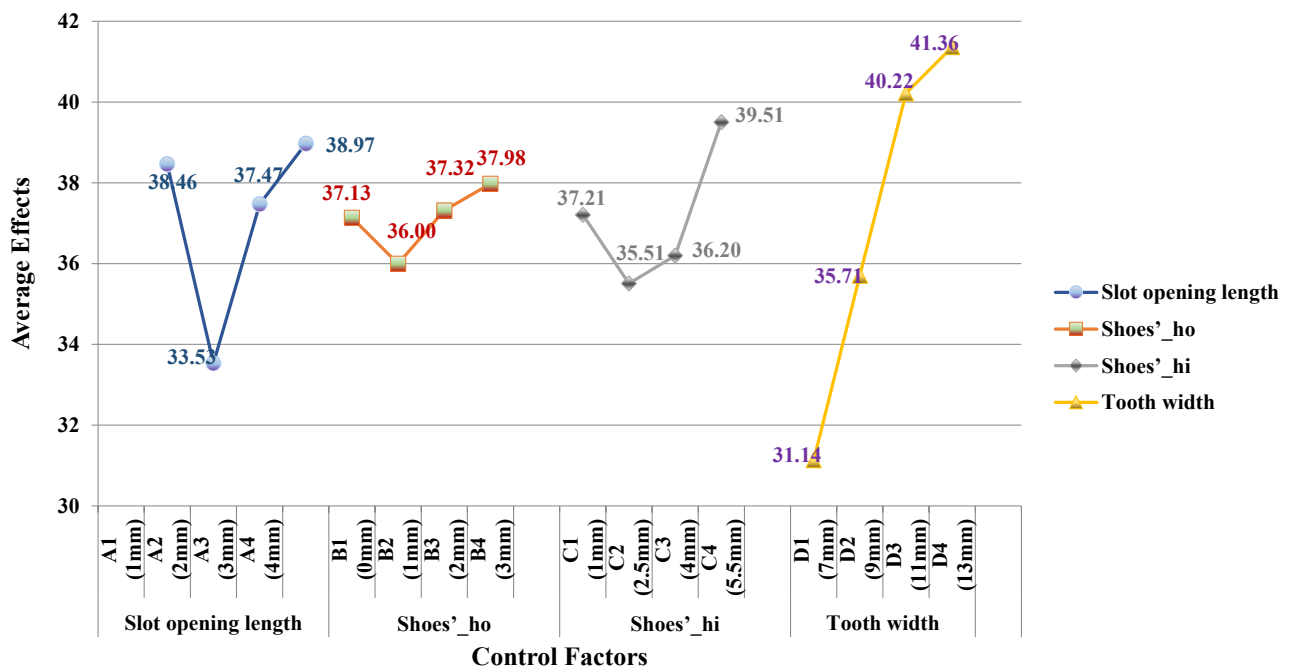
Figure 10. Flux plot of the optimum stator-slot-shoes dimension by Maxwell-2D.
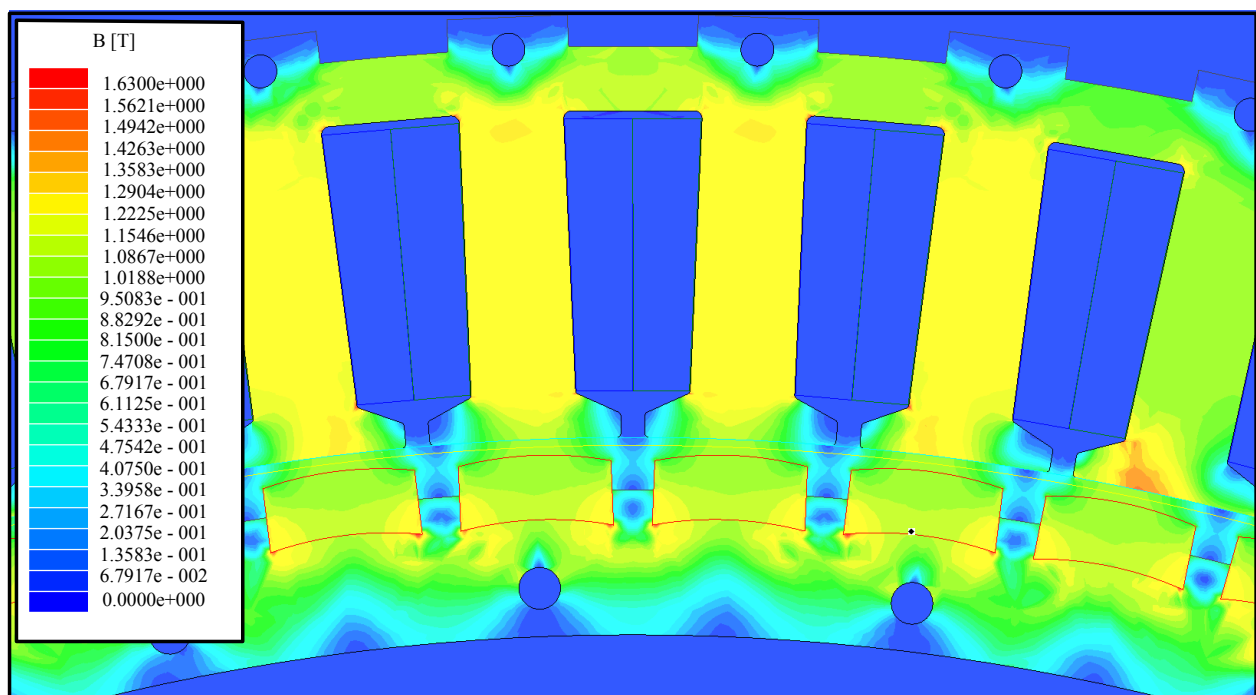
3.3. Finite Element Analysis of the Optimum Case

The electrical characteristics as mentioned refers to the analysis for the induced voltage, which may be further divided into the no-load and load tests. At different rotor speeds the corresponding induced voltage varies, and the rotor speed is proportional to the induced voltage. Furthermore, the induced voltage and current, as well as its output power can be determined at the specific rotor speed by using different loads. In this section, Maxwell-2D is used to analyze PSMG-based electrical characteristics. A Fourier transform with the results by using Matlab is then performed to obtain *THD*.

Based on the optimal parameters obtained above, finite element analysis with Maxwell-2D for 72-slot, 78-pole PMSG under seven different loads is conducted. The rotor is divided into two cylindrical segments of equal length, and adjacent segments are rotated on their axis by a constant angle of the generator. The results for induced voltages and *THD* of double three and six phase winding configurations shown in Table 7 indicate that *THD* of both induced voltage and current are less than 1.4%, complying with IEEE Standard 519.

Table 7. Simulated results by Maxwell-2D.

Parameter		V_p (V)/*THD* (%)		V_l (V)/*THD* (%)		I_p (A)/*THD* (%)		P_o (W)
	No load	208	0.39%	361	0.39%		-	-
	Load 48 Ω	205	0.31%	355	0.31%	4.3	0.33%	2644.50
Double three-phase winding	Load 24 Ω	199	0.31%	345	0.31%	8.3	0.31%	4955.10
	Load 12 Ω	182	0.33%	316	0.33%	15.2	0.33%	8299.20
	Load 6 Ω	146	0.38%	252	0.38%	24.3	0.34%	10643.40
	Load 3 Ω	95	0.82%	164	0.86%	31.6	0.28%	9006.00
	No load	215	1.41%	375	1.39%		-	-
	Load 48 Ω	212	1.20%	355	0.31%	4.4	1.24%	2798.40
Six-phase winding.	Load 24 Ω	206	1.08%	356	1.05%	8.6	1.08%	5314.80
	Load 12 Ω	188	0.95%	336	0.90%	15.7	0.95%	8854.80
	Load 6 Ω	149	0.63%	258	0.64%	24.9	0.63%	11130.30
	Load 3 Ω	97	0.36%	167	0.84%	32.0	0.36%	9312.00

I_p: current per phase.

Figure 11 shows the induced voltages for the electrical angle equaling to 0° between Va_1 and Va_2 for the double three-phase winding; whereas the phase difference between Va and Vx phases is 30° for the six-phase winding. In addition, Table 7 shows that V_p are equal to 208 V and 215 V, respectively, for double three-phase winding and six-phase winding for no-load. This can also be verified from the near-sinusoidal voltage and current waveforms for no-load case from Figure 11. When the speed is 90 rpm, from Table 7, the 6 Ω load receives generator outputs of 10.643 kW and 11.130 kW for the double three-phase winding and six-phase winding, respectively.

Figure 11. Analysis of induced voltage at no-load: (**a**) double three-phase winding; (**b**) six-phase winding.

(**a**)

(**b**)
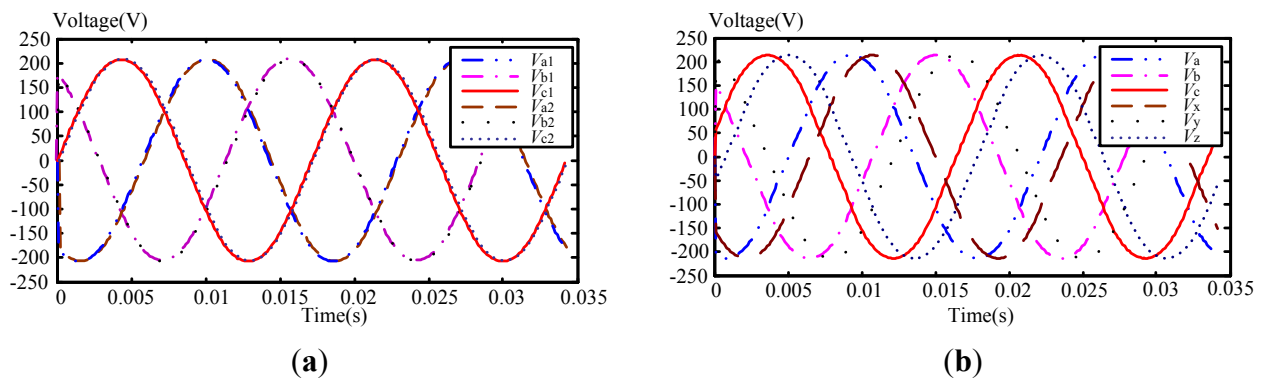
From the frequency domain analysis for V_{a1}, Figure 12 shows that the peak values for V_{a1} under 24 Ω load for the double three-phase winding and six-phase winding are 159.24 V and 160.28 V, respectively, with the corresponding peak values of 7.05 A and 6.43 A for I_{a1}.

Figure 12. Induced voltage and current at 0, 6 and 24 Ω-load: (**a**) double three-phase winding; (**b**) six-phase winding.

(**a**)

(**b**)
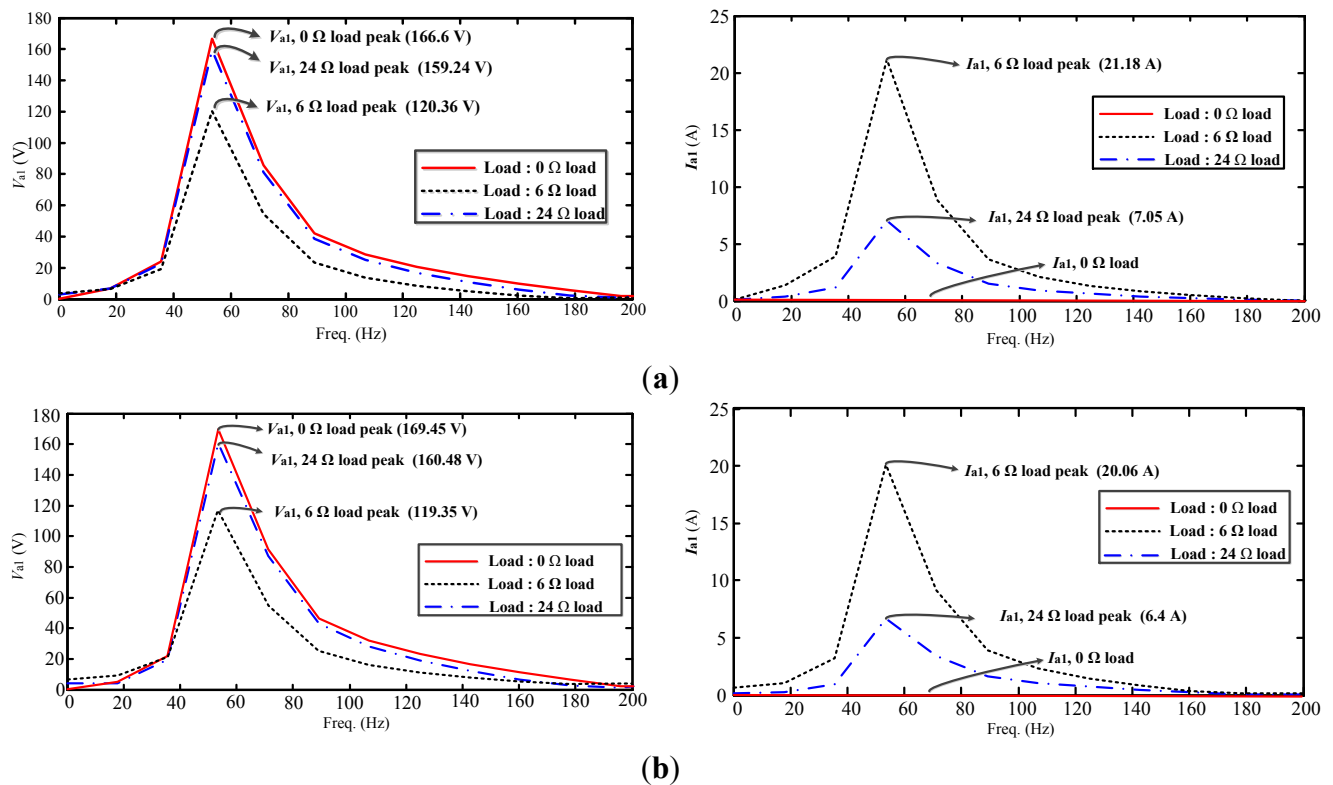
## 4. Experimental Results and Discussion

This section presents the experimental results conducted on the proposed high performance PMSG. The generator and its measurement platform are built and shown in Figure 13, which contains a 6-pole, 50 horsepower (50 hp = 37.3 kW) induction motor as the prime mover.

Figure 13. Experimental apparatus: (**a**) schematic diagram; (**b**) platform photo.

(**a**)

(**b**)
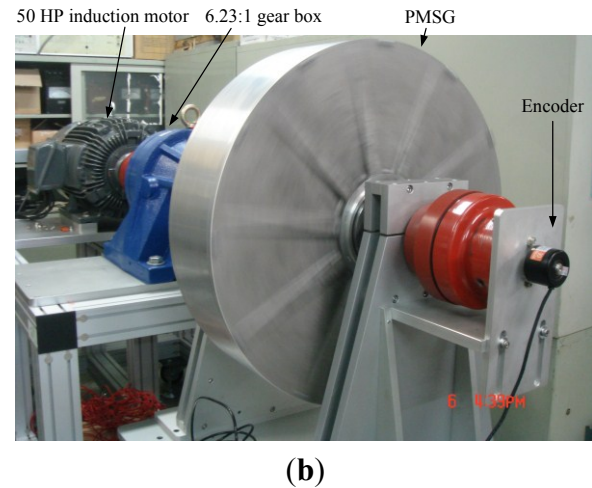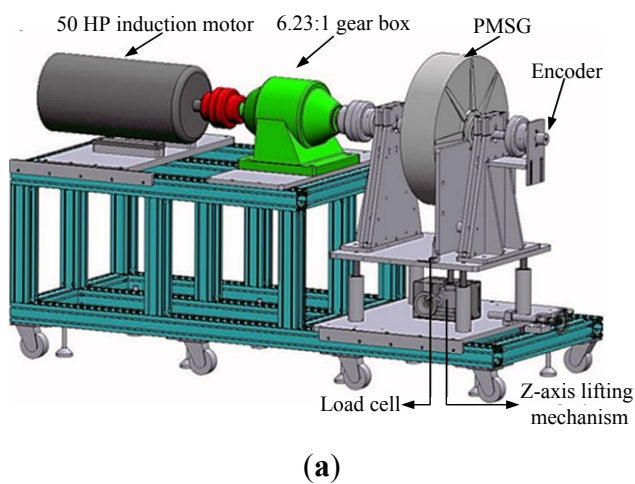
It is seen from Figure 13 that the 72-slot, 78-pole PMSG under test is driven via a reducer with speed ratio of 6.23:1. The wiring of double three-phase and six-phase winding configurations can easily be accomplished through the proposed scheme shown in Figure 14. Calculation of powers and efficiencies using simulated results will be given to compare with the experimental evaluation in this section.

Figure 14. External wiring photo.
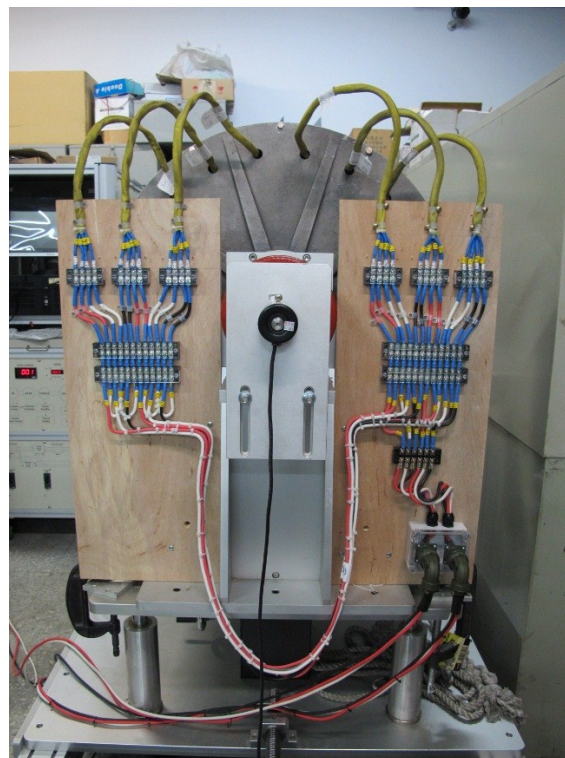
The measured and simulated induced voltages of the PMSG from no-load test for both winding configurations under different speeds are given in Figure 15, where linear relationships between the induced voltage and speed are observed. Besides, Figure 15 also reveals that close agreements for induced voltages between measured and simulated results are obtained. In fact, the differences for both wirings are less than 1%.

Figure 15. Measured and simulated no-load induced voltages: (**a**) double three-phase winding; (**b**) six-phase winding.


(**a**)

(**b**)
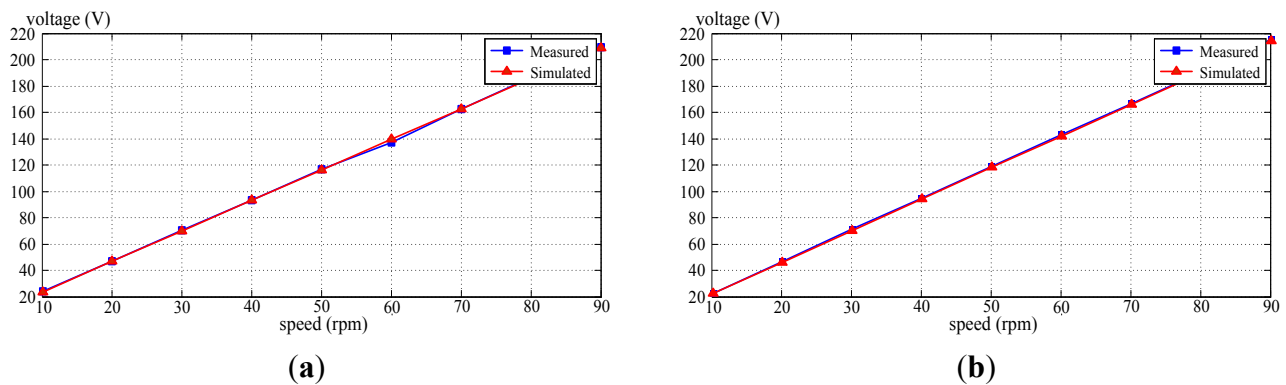
Since the maximum output power of the load box is 5 kW when the generator is operated at rated speed of 90 rpm, the experimental results can only be obtained and compared with simulations for the resistive load of 24 Ω. The experimental results under no-load and 24 Ω load shown in Table 8 indicate that *THD* of the induced line voltages are within 3% for both winding configurations, complying with IEEE Standard 519 as in the simulation case. The corresponding waveforms of the induced voltages given in Figure 16 show near-sinusoidal outputs for no-load case.

Table 8. Measured induced voltages and THD.

Parameter		V_p (V)/*THD* (%)		V_l (V)/THD (%)		I_p (A)/*THD* (%)		P_o (W)
Double three-phase winding	No load	209	0.79%	359	0.59%	-		-
	Load 24 Ω	200	2.82%	344	0.75%	8.1	1.40%	4860
Six-phase winding	No load	217	2.35%	376	2.34%	-		-
	Load 24 Ω	204	3.94%	360	1.92%	8.3	3.45%	5080

Figure 16. Measured no-load induced voltage: (**a**) double three-phase winding; (**b**) six-phase winding.

(**a**)

(**b**)
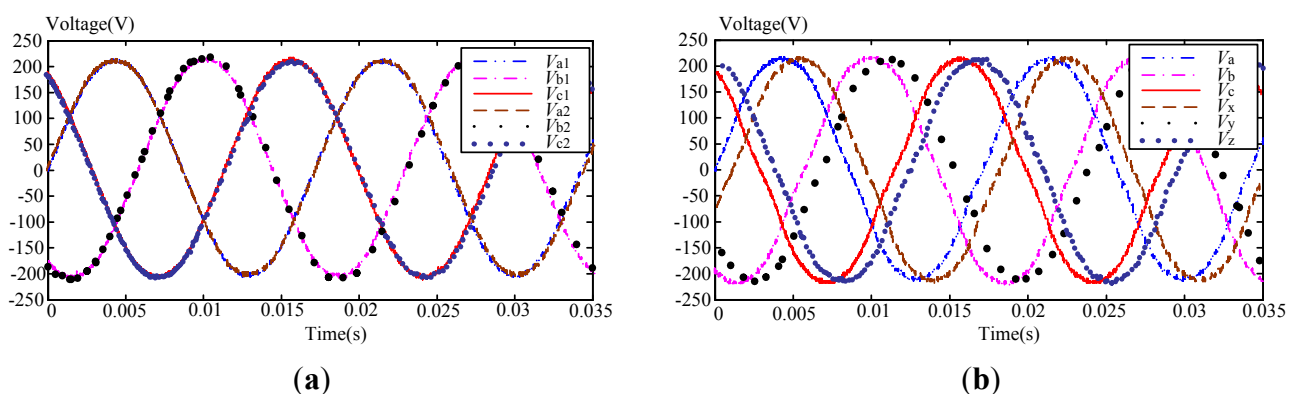
From the frequency domain analysis for V_{a1}, Figure 17 shows that the differences for the peak values of V_{a1} between simulation and experimental results are 7.84 V and 5.94 V for double three-phase winding and six-phase winding, respectively, under 24 Ω load. The corresponding differences for the peak values of I_{a1} between simulation and experimental results are 0.73 A and 0.50 A.

Figure 17. Measured induced voltage and current with 24 Ω load: (**a**) double three-phase winding; (**b**) six-phase winding.

(**a**)

(**b**)
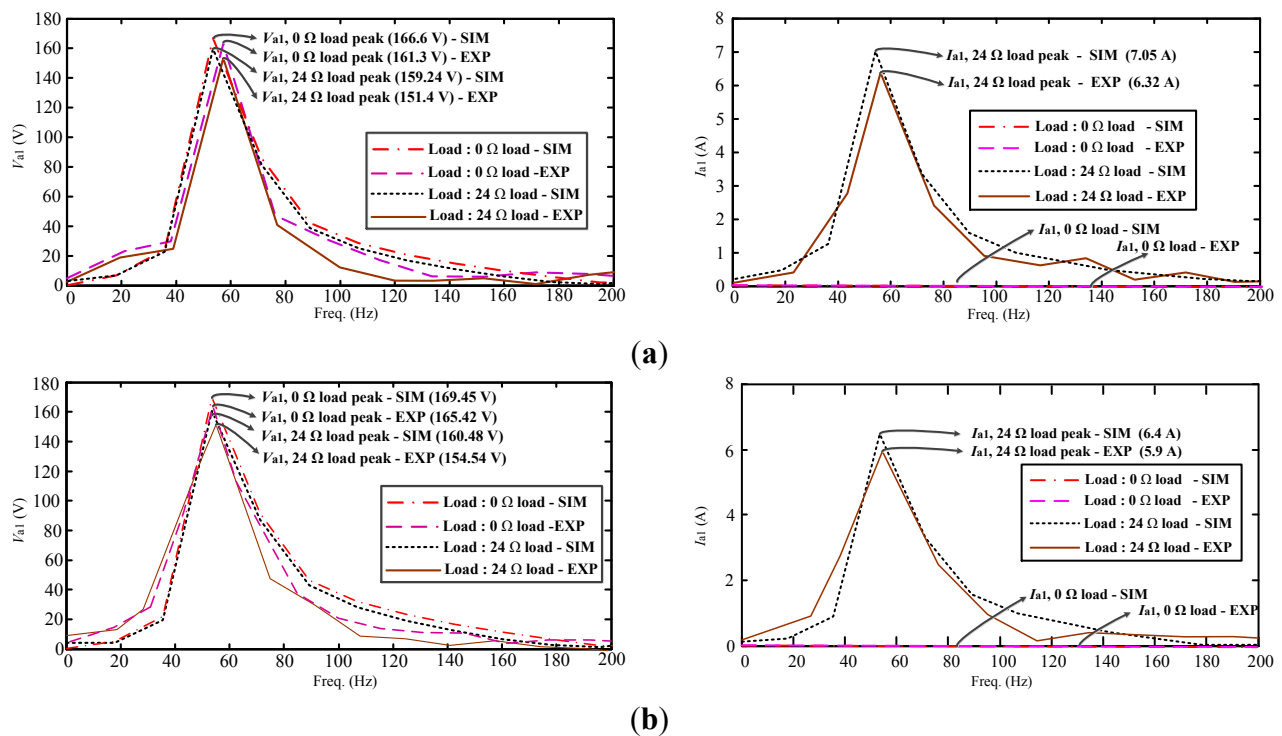
Finally, a load cell installed at the bottom of the generator will yield torques which, in turn, is used to calculate the input and output powers of the generator for the two winding connections. The results are shown in Table 9, which indicates that the output powers of 5.029 and 5.433 kW at 90 rpm for 24 Ω load are obtained with efficiencies of 96.56% and 98.54%, respectively, for double three-phase and six-phase winding.

Table 9. Calculated efficiencies from measured results (Prime mover measured). $V_{l,rms}$: the rms of line induced voltage; $I_{l,rms}$: the rms of line current; ω_m: speed; T: torque; P_o: output power; P_i: input power; η: efficiency.

	$V_{l,rms}$ (V)	$I_{l,rms}$ (A)	ω_m (rpm)	T (kg·m)	P_o (W)	P_i (W)	η (%)
	110	2.7	40	27.10	1028.84	1112.46	92.48
	136	3.4	50	33.30	1601.80	1708.71	93.74
Double three-phase winding	164	4.0	60	39.00	2272.45	2401.43	94.63
	190	4.7	70	45.20	3093.44	3247.07	95.27
	217	5.3	80	50.60	3984.06	4154.27	95.90
	242	6.0	90	56.40	5029.88	5209.26	96.56
	115	2.8	40	28.00	1115.44	1149.40	97.05
	144	3.5	50	34.80	1745.91	1785.68	97.77
Six-phase winding	171	4.2	60	41.20	2487.92	2536.90	98.07
	198	4.9	70	47.60	3360.87	3419.48	98.29
	226	5.5	80	53.30	4305.88	4375.95	98.40
	253	6.2	90	59.70	5433.79	5514.06	98.54

Table 10 compares the aforementioned experimental result from 24 Ω-load with that from Maxwell-2D simulation. It is seen from Table 10 that close agreement between measured and simulated results are also obtained concerning the induced voltages, load currents and output powers.

Table 10. Comprehensive comparison.

Winding connection	Maxwell-2D software					Oscilloscope measured					Prime mover measured				
	No Load		Load 24 Ω			No Load		Load 24 Ω			No Load		Load 24 Ω		
	V_p (V)	I_p (A)	V_p (V)	I_p (A)	P_o (W)	V_p (V)	I_p (A)	V_p (V)	I_p (A)	P_o (W)	V_p (V)	I_p (A)	V_p (V)	I_p (A)	P_o (W)
Double three-phase winding	208	0.0	199	8.3	**4955**	209	0.0	200	8.1	**4860**	212	0.0	198	8.5	**5030**
Six-phase winding	215	0.0	204	8.5	**5315**	217	0.0	204	8.3	**5080**	222	0.0	207	8.8	**5434**

5. Conclusions

This paper presents a systematic and sequential methodology for the design of PMSGs. With the selected $\alpha_{p-p} = 0.800$, zero 3rd and smaller 5th harmonics can be obtained by using Y-connected wiring. As for the Taguchi method, an L_{16} orthogonal array is applied, and 16 simulations and analyses are performed to determine the appropriate control parameters. These include slot-opening length, ho, hi, and tooth width. The selected *S*/*N* ratio is based on increasing the induced voltage and having smaller values of THD and T_B. Under the no-load test, the induced voltage differences between experiment and simulation for both double three-phase winding and six-phase winding are less than 1%. This verifies the reliability of Maxwell 2-D analysis. In addition, 24 Ω load experiments show the output powers of 5.029 kW and 5.433 kW at 90 rpm for double three-phase winding and six-phase winding, respectively. From the results in this study, it can be seen that the PMSG design clearly achieved the proposed high performance features.

Author Contributions

The manuscript is a part of the Ph.D. dissertation of Chun-Yu Hsiao, who had been a Ph.D. student from September 2007 to June 2012, and jointly supervised by Sheng-Nian Yeh, and Jonq-Chin Hwang, Department of Electrical Engineering, National Taiwan University of Science and Technology. The design and analyses of 10 kW PMSG, using FEM and Taguchi method, as well as the experiments were carried out by Hsiao under the supervision and support of both advisors. In addition, the manuscript was first drafted by Hsiao and then revised by Yeh.

Notation

A_m	magnet cross-sectional area
A_g	airgap cross-sectional area
B_g	airgap flux density
B_r	remanence
B_k	k-th harmonic flux ratio

I_p	phase current
$I_{l,rms}$	rms of line current
K_l	leakage factor
k_h	the k-th harmonic
K_r	reluctance factor
l_m	magnet thickness
l_g	airgap length
P_c	permeance coefficient
P_o	output power
P_i	Input power
$\mathfrak{R}_l$	leakage magnetic reluctance
$\mathfrak{R}_r$	rotor steel reluctance
$\mathfrak{R}_s$	stator steel reluctance
$\mathfrak{R}_g$	airgap reluctance
$\mathfrak{R}_m$	magnet reluctance
R_{si}	Stator inside radius
R_{so}	Stator outside radius
R_{ri}	Rotor inside radius
R_{ro}	Rotor outside radius
T	torque
V_p	phase induced voltage
V_l	line induced voltage
$V_{l,rms}$	rms of line induced voltage
ϕ_g	airgap flux
ϕ_r	Magnet remanent flux
ϕ_l	Leakage flux
μ_r	relative permeability
μ_0	permeability of free space
$\alpha_{p\text{-}p}$	The ratio between the width of the magnet and the pole-pitch of rotor core
α_{arc}	pole-arc
α_{pitch}	pole-pitch
θ_e	electrical degree
ω_m	speed
η	efficiency

Conflicts of Interest

The authors declare no conflicts of interest.

References

1. Bumby, J.R.; Stannard, N.; Dominy, J.; McLeod, N. A permanent magnet generator for small scale wind and water turbines. In Proceedings of the International Conference on Electrical Machines, Vilamoura, Portugal, 6–9 September 2008; pp. 1–6.
2. Maia, T.A.C.; Faria, O.A.; Cardoso, A.A.R.F.E.; Borges, F.S.; Mendonca, H.G.; Silva, M.A.; Vasconcelos, J.A.; Silva, S.R.; Lopes, B.M. Electromechanical design for an optimized axial flux permanent magnet torus machine for 10 kW wind turbine. In Proceedings of the International Conference on Electrical Machines and Systems, Beijing, China, 20–23 August 2011; pp. 1–6.
3. He, Q.; Wang, Q. Optimal design of low-speed permanent magnet generator for wind turbine application. In Proceedings of the Asia-Pacific Power and Energy Engineering Conference, Shanghai, China, 27–29 March 2012; pp. 1–3.
4. Eriksson, S.; Solum, A.; Leijon, M.; Bernhoff, H. Simulations and experiments on a 12 kW direct driven PM synchronous generator for wind power. *Renew. Energy* **2008**, *33*, 674–681.
5. Eriksson, S.; Bernhoff, H.; Bergkvist, M. Design of a unique direct driven PM generator adapted for a telecom tower wind turbine. *Renew. Energy* **2012**, *44*, 453–456.
6. Chalmers, B.J.; Wu, W.; Spooner, E. An axial-flux permanent-magnet generator for a gearless wind energy system. *IEEE Trans. Energy Conv.* **1999**, *14*, 251–257.
7. Sadeghierad, M.; Darabi, A.; Lesani, H.; Monsef, H. Rotor yoke thickness of coreless high-speed axial-flux permanent magnet generator. *IEEE Trans. Magn.* **2009**, *45*, 2032–2037.
8. Chaar, L.E.; Lamont, L.A.; Elzein, N. Wind energy technology-industrial update. In Proceedings of the IEEE Power and Energy Society General Meeting, Detroit, MI, USA, 24–29 July 2011; pp. 1–5.
9. Chan, T.F.; Lai, L.L.; Xie, S. Field computation for an axial flux permanent-magnet synchronous generator. *IEEE Trans. Energy Convers.* **2009**, *24*, 1–11.
10. Caricchi, F.; Maradei, F.; de Donato, G.; Capponi, F.G. Axial-flux permanent magnet generator for induction heating gensets. *IEEE Trans. Ind. Electron.* **2009**, *57*, 128–137.
11. Hwang, J.C.; Hsiao, C.Y.; Yeh, S.N. Composite Permanent Magnet Synchronous Machine. U.S. Patent No. 13/452,465, 20 April 2014.
12. Hanselman, D. *Brushless Permanent Magnet Motor Design*; Magna Physics Pub.: Orono, ME, USA, 2003.
13. Zhu, Z.Q.; Howe, D. Influence of design parameters on cogging torque in permanent magnet machines. *IEEE Trans. Energy Convers.* **2000**, *15*, 407–412.
14. Phadke, M.S. *Quality Engineering Using Robust Design*; Prentice Hall: Upper Saddle River, NJ, USA, 1995.
15. Ross, P.J. *Taguchi Techniques for Quality Engineering*; McGraw-Hill Book Company: New York, NY, USA, 1998.
16. Lee, H.H. *Taguchi Methods: Principles and Practices of Quality Design*; Gau Lih Book Company Ltd.: Taipei, Taiwan, 2011.
17. Kim, W.H.; Kim, K.C.; Kim, S.J.; Kang, D.W.; Go, S.C.; Lee, H.W.; Chun, Y.D.; Lee, J. A study on the optimal rotor design of LSPM considering the starting torque and efficiency. *IEEE Trans. Magn.* **2009**, *45*, 1808–1811.

18. Awada, A.; Wegmann, B.; Viering, I.; Klein, A. Optimizing the radio network parameters of the long term evolution system using Taguchi's method. *IEEE Trans. Veh. Technol.* **2011**, *60*, 3825–3839.

19. Hwang, C.C.; Li, P.L.; Liu, C.T. Optimal design of a permanent magnet linear synchronous motor with low cogging force. *IEEE Trans. Magn.* **2012**, *48*, 1039–1042.

20. Shi, T.; Qiao, Z.; Xia, C.; Li, H.; Song, Z. Modeling, analyzing, and parameter design of the magnetic field of a segmented Halbach cylinder. *IEEE Trans. Magn.* **2012**, *48*, 1890–1898.

21. Gologlu, C.; Sakarya, N. The effects of cutter path strategies on surface roughness of pocket milling of 1.2738 steel based on Taguchi method. *J. Mater. Process. Technol.* **2008**, *206*, 7–15.

22. Esme, U.; Bayramoglu, M.; Kazancoglu, Y.; Ozgun, S. Optimization of weld bead geometry in TIG welding process using grey relation. *Int. J. Eng. Res. Appl.* **2009**, *43*, 143–149.